Dependence of guided resonances on the structural parameters of terahertz photonic crystal slabs

Tushar Prasad,[1] Vicki L. Colvin,[1] and Daniel M. Mittleman[2,*]

[1]*Department of Chemistry, Rice University, MS-60, 6100 Main Street, Houston, Texas 77005, USA*
[2]*Department of Electrical & Computer Engineering, Rice University, MS-366, 6100 Main Street, Houston, Texas 77005, USA*
**Corresponding author: daniel@rice.edu*

Received December 18, 2007; accepted January 24, 2008;
posted February 13, 2008 (Doc. ID 90908); published March 31, 2008

Using terahertz spectroscopy, we measure the normal-incidence transmission coefficient of photonic crystals consisting of a periodic lattice of air holes in a silicon slab. Sharp resonant features are observed in the transmission spectra due to coupling of the leaky photonic crystal modes, called guided resonances, to the continuum of free-space modes. The resonances show considerable sensitivity to the structural parameters of the slab, including the slab thickness. By varying each crystal parameter systematically, we study the dependence of the resonances on the geometry of the photonic crystal slabs. Even small changes in a parameter such as the slab thickness, for example, can lead to dramatic changes in the optical spectrum. We also compare the transmission spectrum of a photonic crystal slab with a hexagonal lattice to that of a slab with a square lattice. In most cases, the experimental results match very well with numerical simulations based on the finite element method.

OCIS codes: 160.5298, 300.6495.

1. INTRODUCTION

Photonic crystals are materials with a periodically modulated refractive index in one or more dimensions [1]. They have been studied extensively due to their potential to manipulate the propagation of electromagnetic waves in a variety of novel ways [2,3]. In particular, photonic crystal slabs have attracted a great deal of attention because they provide a route toward the development of optical architectures for integrated photonic circuits [4]. A photonic crystal slab has a two-dimensional lattice structure in the plane of the slab and uses index guiding to confine light in the third dimension.

In the band structure of a photonic crystal slab, the modes that lie below the light line are strictly confined in the plane of the slab. These in-plane modes, called guided modes, have been exploited to implement various photonic devices [5–11]. In contrast to the guided modes, the photonic crystal modes that lie above the light line can leak out of the plane of the slab. These discrete leaky modes, called guided resonances, couple to the continuum of free-space modes to produce sharp resonant features in the out-of-plane transmission spectrum of the photonic crystal slab [12–14]. The resonant features exhibit an asymmetrical line shape [15], characteristic of the well-known Fano resonance phenomenon observed in condensed matter systems due to interference between discrete and continuum states [16,17].

Guided resonances have been the topic of much recent research. Several studies have exploited the leaky modes in photonic crystal slabs to realize efficient light emitting devices [18–20]. The Fano resonances in photonic crystal slabs have been used to demonstrate mirrors and polarization splitters [21] and also to describe high transmission through sharp bends [22]. It has been shown that by varying the distance between a pair of closely spaced photonic crystal slabs, the guided resonances can be tuned to design optical switches, displacement sensors, and optical filters [23–25]. Reports on the observation of guided resonances in asymmetrical photonic crystal slabs are very promising because of the ease of fabrication of such structures [26]. Some studies have analyzed the characteristics of guided resonances in crystal lattices with a structural disorder [27,28]. The dependence of guided resonances on the angle of illumination was studied in photonic crystal slabs at visible, near-infrared, and terahertz frequencies [29–31]. A recent theoretical study used electron injection, electric field, and temperatures to control the Fano resonance shift in photonic crystal slabs [32]. More recently, Grillet *et al.* used air-hole photonic crystal slabs to study the properties of guided resonances as a function of the hole radius [33]. However, a systematic study of the variation of the optical spectra as a function of structural parameters is still lacking.

In this paper, we present experimental and theoretical studies of guided resonances in terahertz photonic crystal slabs as a function of various crystal parameters. The photonic crystal slabs are fabricated by etching an array of holes in silicon. For most of the data presented in this paper, normal-incidence transmission spectra are obtained using terahertz time-domain spectroscopy [34,35]. As the crystal parameters such as the hole radius, the lattice periodicity, and even the slab thickness are changed,

the resonant features in the transmission spectrum vary significantly. A comparison between the transmission spectra of photonic crystal slabs with hexagonal and square lattices of holes is also presented. The observations show that the guided resonances are very sensitive to the lattice geometry of the crystal.

Our results also highlight the excellent correspondence between experimental measurements and numerical calculations based on the finite element method (FEM). Such agreement is notable, particularly for photonic bands lying above the light line, because these bands are very difficult to compute accurately for the case of a two-dimensional slab of finite thickness using plane wave expansion methods [36]. In our case, careful comparisons are possible because the photonic crystals are fabricated with essentially no structural disorder and negligible surface roughness effects [28].

2. EXPERIMENT

A schematic of the experimental setup is shown in Fig. 1. Single-cycle terahertz pulses are generated and detected using photoconductive antennas. To measure the normal-incidence transmission spectrum, the photonic crystal slab is placed perpendicular to the beam path. The terahertz radiation is focused into the crystal by a polyethylene lens, and a similar setup is used to collect the transmitted radiation. The spot size of the terahertz beam on the sample is roughly 8 mm, so many holes are illuminated. Using this technique, one measures the transmitted electric field as a function of time. The complex transmission coefficient of a sample is given by the ratio of the Fourier transform of a pulse transmitted through the sample to that of a reference. The reference is the freely propagating pulse measured without the sample in the beam path. This also permits a direct measurement of the spectral phase of the transmitted radiation relative to that of the reference pulse [31]. By measuring the terahertz pulse over a 555 ps window, a frequency resolution of 1.8 GHz is obtained in the measurements. To obtain a higher spectral resolution, we used a spectrometer based on a backward-wave oscillator (BWO) source as described in Subsection 5.D.

The photonic crystal slabs consist of a hexagonal array of circular air holes in silicon. A slab with a square lattice of holes was also fabricated for a comparison of the transmission spectra. The holes are etched all the way through

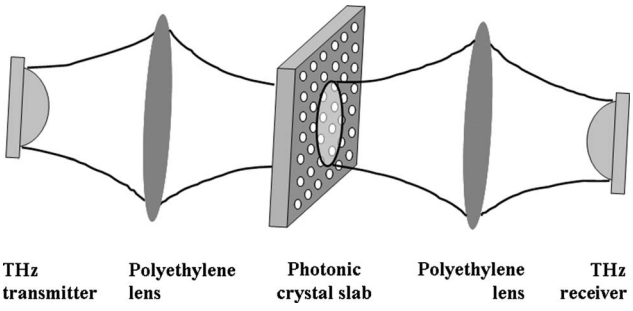

Fig. 1. Schematic of the experimental setup. The terahertz radiation propagates in the direction perpendicular to the plane of the photonic crystal slab. The terahertz beam spot size is ~8 mm.

the silicon slab using deep reactive ion etching [35,37,38]. Silicon of very high resistivity ($\rho > 10\ \mathrm{k\Omega\ cm}$) is used because of its low absorption and frequency-independent refractive index ($n = 3.418$) in the terahertz regime [39]. Each photonic crystal slab is characterized by three parameters, the hole radius r, the lattice parameter a, and the slab thickness t. Figure 2(a) shows one of the samples, with $r = 150$, $a = 400$, and $t = 300\ \mu\mathrm{m}$. In all measurements presented in this paper, the electric field is polarized along the Γ-K direction of the hexagonal lattice, although identical results are obtained for the Γ-M orientation as well. For the slab with a square lattice, the electric field is polarized along the Γ-X direction.

As the feature sizes in the fabricated crystals are on the order of several hundred micrometers, it is possible to fabricate essentially perfect crystals using standard lithographic and etching techniques. For example, a careful analysis of the variation in hole diameters across an ~1 cm area of a wafer reveals a $< \pm 0.3\%$ variation [28], where this uncertainty ($\pm 1\ \mu\mathrm{m}$) corresponds to the resolution of our optical imaging system and is therefore an upper bound. This high sample quality is important for quantitative comparisons with numerical simulations.

Figure 2(b) shows the normal-incidence transmission spectrum for the sample shown in Fig. 2(a). The spectrum consists of sharp resonant features superimposed upon a smoothly varying background. The smoothly varying background is due to the Fabry–Perot oscillations that arise because of the finite slab thickness. They appear as an oscillatory transmission below 0.4 THz. The sharp features in the spectrum above 0.4 THz are signatures of the leaky photonic crystal modes that are excited due to normal-incidence illumination of the crystal. The widths of these resonant features represent the lifetimes of the modes. These linewidths are determined by the details of the photonic band structure, which in turn depends sensitively on the structural parameters of the slab. They can be as narrow as only a few hundred megahertz (see Fig. 15 below) or as broad as several tens of gigahertz. The overall spectrum is the superposition of the Fabry–Perot oscillations and the leaky photonic crystal modes. We see that the experimental results match very well with the finite element simulations, confirming that the fabricated crystals are of essentially perfect quality.

3. NUMERICAL MODELING

The theoretical transmission spectra shown throughout this paper are obtained using simulations based on the FEM. This technique has been successfully used to analyze various photonic crystal properties [31,40,41] as well as other phenomena in the terahertz range [42,43]. The accuracy of the FEM is closely related to the quality of discretization of the model geometry. Finer discretization of the structure produces more accurate solutions but also requires large amounts of computer memory. Therefore, it is important to construct a model geometry that not only represents the structure accurately but can also be simulated using the available computational resources. The dashed rectangle in the bottom picture of Fig. 3 depicts the smallest unit cell of the photonic crystal slab with a hexagonal lattice. By defining the boundary conditions

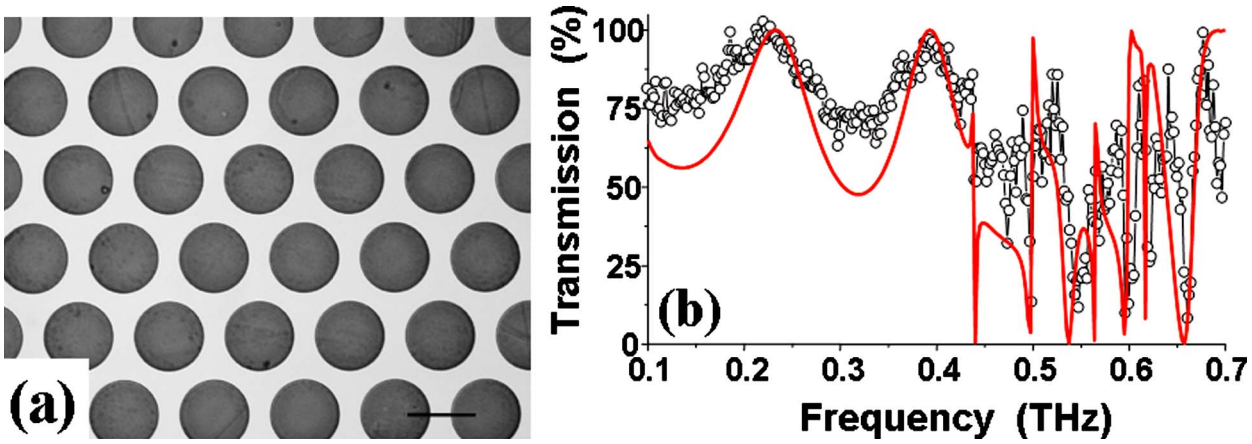

Fig. 2. (Color online) (a) Top view of the photonic crystal slab with a hexagonal lattice of air holes. The crystal parameters are $r=150$, $a=400$, and $t=300$ μm. The scale bar is 300 μm. (b) Normal-incidence transmission spectrum of the photonic crystal slab shown in (a). The open circles are experimental results while the solid curve is obtained from simulations based on the FEM.

appropriately, this symmetrical rectangular part can describe the two-dimensional periodicity in the plane of the slab. The top picture in Fig. 4 shows the computational domain that was constructed to calculate the normal-incidence transmission spectrum. The thickness of the unit cell is specified as t, the slab thickness. Depending on the crystal being simulated, the hole radius r and the lattice parameter a are appropriately defined in the model. The refractive index of the hole and the silicon are assigned as 1.00 and 3.418, respectively. Air regions of cross sections similar to the unit cell are placed before and after the unit cell. Accurate results are obtained for the relevant frequency range when the thicknesses of these air regions are at least four times that of the unit cell. The top and bottom boundaries of the whole model are defined as perfect electric conductors while the side boundaries are defined as perfect magnetic conductors. This ensures that the electromagnetic energy within the model is not lost due to absorption. It also establishes the symmetry of the unit cell required for an accurate description of the in-plane periodicity of the photonic crystal slab. The whole structure is discretized using a mesh of 20 μm in size, which results in a model with roughly 600,000 mesh elements. The arrow shown in the computational domain (Fig. 3) indicates the direction in which the electromagnetic radiation propagates. The electric field is polarized along the Γ-M direction of the hexagonal lattice, although similar results are obtained for the Γ-K polarization. (The model geometry for the square lattice photonic crystal is described in Section 6.) The normal-incidence transmission coefficient is obtained by taking the ratio of the integrated power at the output plane to that at the input plane. One can also calculate the phase at the output plane and obtain the relative phase by subtracting the phase of the reference (model with no sample in the beam path) from that of the sample. For a frequency resolution of 2 GHz over the spectral range of interest (0.1–0.7 THz), a typical model runs in ~22 h on a dual-processor workstation equipped with 16 Gbytes of RAM. Although computationally cumbersome, this method provides an extremely accurate simulation of the experiment.

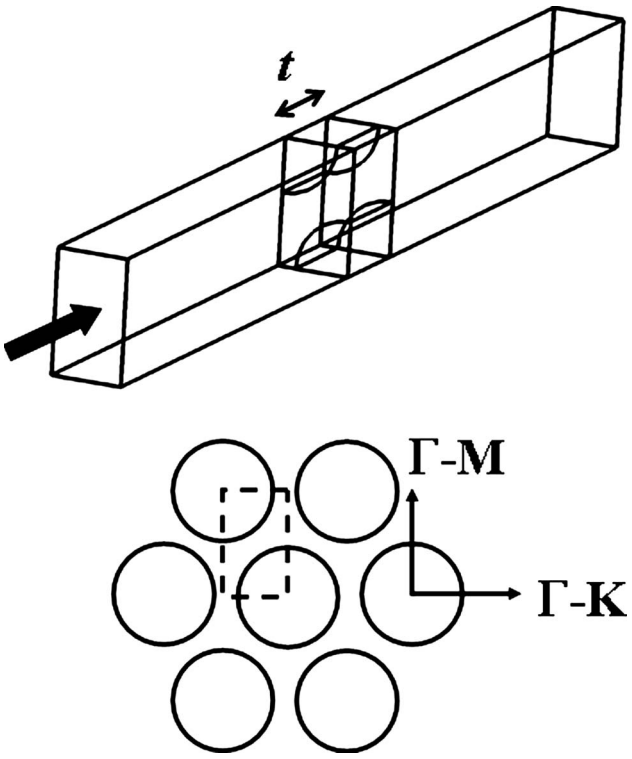

Fig. 3. Top, FEM model for the hexagonal lattice photonic crystal. The electromagnetic radiation propagates in the direction indicated by the arrow; t is the slab thickness. Bottom, hexagonal lattice with high-symmetry directions marked. The dashed rectangle is a cross section of the smallest unit cell used in the FEM simulations.

4. LINE SHAPE ANALYSIS

The spectrum shown in Fig. 2(b) consists of sharp resonant features superimposed upon a smoothly varying background. The smoothly varying Fabry–Perot oscillations that form the background are more obvious at lower frequencies below the frequency of the first guided resonance at ~0.44 THz. The spacing between the successive minima (or maxima) in the Fabry–Perot oscillations is

governed by the thickness and the average refractive index of the slab. The sharp features in the spectrum above 0.44 THz are manifestations of the guided resonance modes of the photonic crystal slab. These discrete guided resonance modes couple to the continuum of the free-space modes to produce transmission line shapes with a Fano profile [14]. The transmission line shape of the guided resonance is asymmetrical in nature and can be written as [15,31]

$$t_{\mathrm{GR}_j}(\omega) = \frac{\rho - \tau \cdot \Omega_j(\omega)}{1 + i\Omega_j(\omega)}, \tag{1}$$

where $\rho=(\tilde{n}-1)/(\tilde{n}+1)$ is the amplitude reflection coefficient calculated using the average refractive index ($\tilde{n}$) of the photonic crystal slab. For a hexagonal lattice of air holes in silicon with $r=150$ and $a=400$ μm, the average refractive index of the slab is $\tilde{n}=2.497$ [Eq. (6)]. τ is the amplitude transmission coefficient such that $\tau^2=1-\rho^2$. The normalized frequency, Ω_j, for the jth resonance is given by

$$\Omega_j(\omega) = \frac{\omega - \omega_j}{\gamma_j}, \tag{2}$$

where ω_j and γ_j are the resonant frequency and the linewidth of the jth resonance, respectively. The overall transmission is the superposition of the Fabry–Perot response and the transmission due to the individual guided resonances:

$$t(\omega) = t_{\mathrm{FP}}(\omega) + t_{\mathrm{GR}_1}(\omega) + t_{\mathrm{GR}_2}(\omega) + t_{\mathrm{GR}_3}(\omega) + \cdots, \tag{3}$$

$$t(\omega) = t_{\mathrm{FP}} + \sum_{j=1}^{\mathrm{N}} \frac{\rho - \tau \cdot \Omega_j(\omega)}{1 + i\Omega_j(\omega)}. \tag{4}$$

Each resonant feature in the experimental transmission spectrum can be described by an appropriate choice of two parameters, ω_j, the resonant frequency, and γ_j, the corresponding linewidth. Table 1 shows the best-fitted values of ω_j and γ_j for the first seven guided resonances in the spectrum shown in Fig. 2(b). The Fabry–Perot response is calculated using the known thickness of the slab ($t=300$ μm) and the frequency-independent average refractive index ($\tilde{n}=2.497$). The overall transmission spectrum is obtained from Eq. (4) by substituting Eq. (2) and using $N=7$. For the choice of fitting parameters shown in Table 1, the line shapes predicted by the simple analytical model of Eq. (4) agree reasonably well with the experimental line shapes (see Fig. 4).

Table 1. Resonant Frequencies (ω_j) and the Corresponding Linewidths (γ_j) of the First Seven Guided Resonances Shown in Fig. 2(b)[a]

Resonance	ω_j (THz)	γ_j (GHz)
1	0.43918	0.05
2	0.49858	0.08
3	0.54358	4.00
4	0.55617	1.00
5	0.59377	10.0
6	0.62097	0.65
7	0.65957	1.20

[a]These values are used to obtain the normalized frequency parameter Ω_j [from Eq. (2)] for each resonance, and subsequently, the transmission spectrum [from Eq. (4)] shown in Fig. 4.

5. DEPENDENCE OF THE RESONANCES ON THE STRUCTURAL PARAMETERS

To harness the full potential of the guided resonances for various applications, it is important to characterize their properties. Several studies have analyzed the guided resonances in photonic crystal slabs as a function of the angle of illumination [29–31]. Theoretical as well as experimental studies have shown that the linewidths of the resonances can be controlled by varying the radii of the holes [14,33]. While there are theoretical predictions on how the guided resonances would change as the lattice parameter and the slab thickness are varied [30,44], experimental demonstrations have not been reported. We study the properties of guided resonances in photonic crystal slabs for a systematic change in each crystal parameter, the hole radius r, the lattice parameter a, and the slab thickness t.

A. Effect of Change in the Hole Radius r

Figure 5 shows the transmission spectra of three photonic crystal slabs, each with a different hole radius r. The lattice parameter a and the slab thickness t are identical for all the samples, $a=400$ and $t=300$ μm. The photonic crystal slabs have a hexagonal lattice of holes, and the hole radii of the samples in Fig. 5 are (a) 180, (b) 150, and (c) 125 μm. The corresponding r/a ratios are 0.45, 0.375, and 0.3125, respectively. It is evident that the resonances shift to lower frequencies as the radius is decreased. As the r/a ratio decreases, the average refractive index of the slab increases [see Eq. (6)]. An increase in the average refractive index of the slab moves the photonic bands to lower frequencies. As a result, the resonances in the transmission spectra appear at lower frequencies. Another clearly evident feature is that the decrease in the hole radius causes the resonances to be sharper, signifying an increase in their lifetime within the slab. This is expected since all resonances asymptotically become true guided modes as the hole radius approaches zero. Similar effects have been discussed in previous papers [14,30,33].

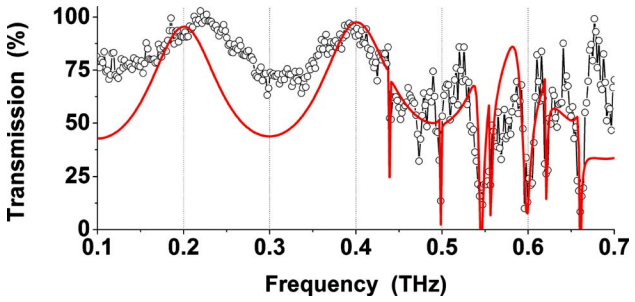

Fig. 4. (Color online) Same as Fig. 2(b) except that the solid curve is obtained from an analytical expression [Eq. (4)], using the parameters given in Table 1.

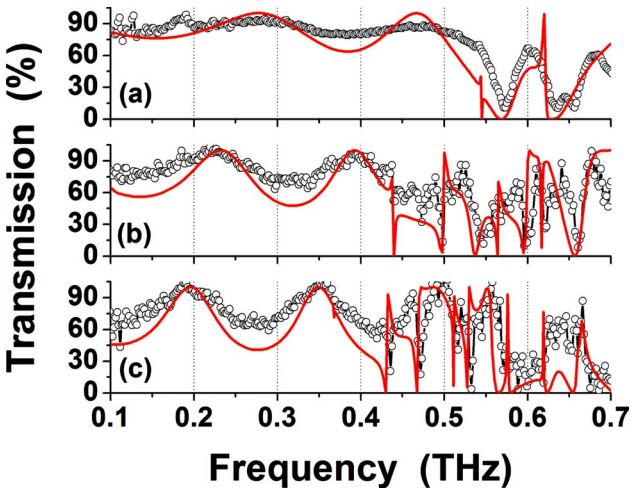

Fig. 5. (Color online) Variation of guided resonances with the hole radii r. Normal-incidence transmission spectra of photonic crystal slabs with (a) $r=180$, (b) $r=150$, and (c) $r=125\ \mu$m. The lattice parameter and slab thickness are identical for all the samples, $a=400$ and $t=300\ \mu$m. The open black circles are experimental results while the solid curves are results of FEM simulations. The theoretical spectrum in (c) matches well with the experimental spectrum when $t=296\ \mu$m is used in the simulation.

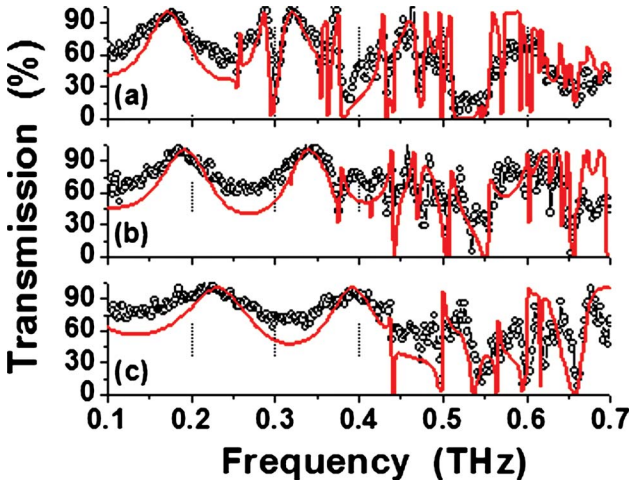

Fig. 6. (Color online) Variation of guided resonances with the lattice parameter a. Normal-incidence transmission spectra of photonic crystal slabs with (a) $a=575$, (b) $a=480$, and (c) $a=400\ \mu$m. The hole radius and slab thickness are identical for all the samples, $r=150\ \mu$m and $t=300\ \mu$m. The open circles are experimental results while the solid curves are results of FEM simulations.

B. Effect of Change in the Lattice Parameter *a*

Figure 6 shows the transmission spectra of three photonic crystal slabs, each with a different lattice parameter a. The hole radius r and the slab thickness t are identical for all the samples, $r=150$ and $t=300\ \mu$m. The photonic crystal slabs have a hexagonal lattice of holes, and the lattice parameters of the samples in Fig. 6 are (a) 575, (b) 480, and (c) 400 μm. The corresponding r/a ratios are 0.26, 0.3125, and 0.375, respectively. Figure 6(c) is the same as Fig. 5(b). As the lattice parameter decreases, the resonances shift to higher frequencies for reasons similar to those mentioned in connection with Fig. 5.

From Figs. 5 and 6, it is clear that if the slab thickness is kept constant, then the shift in the spectral positions of the guided resonances due to a change in either the hole radius or the lattice parameter can be partially understood by examining the corresponding change in the average refractive index, or equivalently, the r/a ratio. Subsection 5.C combines the results of Figs. 5 and 6 to analyze the variation in the positions of the guided resonances as a function of the r/a ratio.

C. Effect of Change in the *r*/*a* Ratio

Figure 7(a) summarizes the observed shift in the positions of the first three guided resonances as a function of the r/a ratio. The positions of the resonances for each sample are extracted from Figs. 5 and 6. The shift in the position of each resonance is approximately linear with respect to the r/a ratio as depicted by the linear fits. For $r/a=0.45$, the position of the first resonance is not shown. Although present in the calculated spectrum [Fig. 5(a)], this resonance is not observed in the experimental spectrum, possibly because its linewidth (~1 GHz as per the calculation) is less than the resolution of the measurements. Figure 7(b) shows the filling fraction of the hexagonal lattice of holes (ϕ_h) and the average refractive index of the photonic crystal slab ($\tilde{n}$) as a function of the r/a. The curves are obtained from the relations

$$\phi_h = \frac{2\pi}{\sqrt{3}}\left(\frac{r}{a}\right)^2, \tag{5}$$

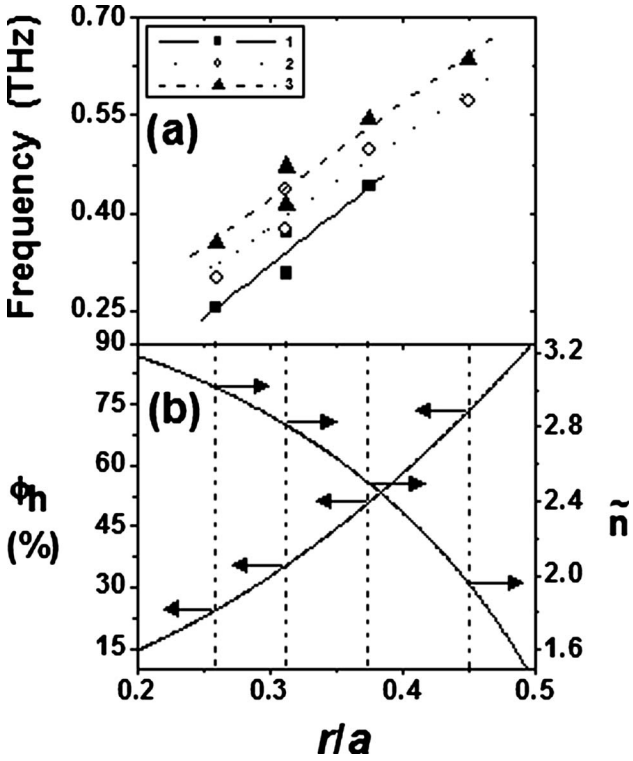

Fig. 7. (a) Shifts in the positions of the first three resonances as a function of r/a (extracted from Figs. 5 and 6). (b) (left) Variation of the filling fraction of the air holes and (right) the average refractive index of the photonic crystal slab as a function of the r/a value of the hexagonal lattice. The dashed vertical lines depict the r/a values of the samples whose transmission spectra are shown in Figs. 5 and 6.

Table 2. Shifts in the Positions of the First Three Resonances for a 2% Change in the r/a Ratio, the Hole Radius, and the Lattice Parameter[a]

	Shift in Resonance 1 (GHz)	Shift in Resonance 2 (GHz)	Shift in Resonance 3 (GHz)	Change in ϕ_h (%)	Change in $\tilde{n}$ (%)
2% change in r/a, from 0.3125	10.07 (3.0% change)	8.71 (2.2% change)	9.28 (2.1% change)	4.04	0.98
2% change in r, from 150 μm ($a=400$ μm)	12.10 (2.7% change)	10.46 (2.2% change)	11.14 (2.1% change)	4.04	1.81
2% change in a, from 400 μm ($r=150$ μm)	11.86 (2.8% change)	10.24 (2.2% change)	10.91 (2.1% change)	4.04	1.68

[a]These values are extracted from the best-fitted linear curves shown in Fig. 7(a). Corresponding changes in the filling fraction of the air holes and the average refractive index of the photonic crystal slab are obtained from Eqs. (5) and (6).

$$\tilde{n} = \sqrt{(\varepsilon_{Si} \times \phi_{Si}) + (\varepsilon_h \times \phi_h)}, \quad (6)$$

where $\varepsilon_{Si}=11.68$, $\varepsilon_h=1.00$, and $\phi_{Si}=1-\phi_h$. The dashed vertical lines are the r/a ratios of the different samples whose transmission spectra are shown in Figs. 5 and 6 and correspond to $r/a=0.26$, 0.3125, 0.375, and 0.45.

Using the linearly fitted curves in Fig. 7(a), the shift in the first three resonances can be quantified with respect to small changes in the r/a ratio. Table 2 summarizes the shifts in the positions of the resonances and the corresponding changes in ϕ_h and $\tilde{n}$ for small changes in the crystal parameters. The first row in Table 2 shows that a 2% change in the r/a value from 0.3125 shifts the resonance positions by 2%–3%. It also changes the filling fraction of the holes by ~4% and the average refractive index of the slab by ~1%. If the hole radius is $r=125$ μm and the lattice parameter is $a=400$ μm (such that $r/a=0.3125$), then a 2% change in the hole radius (keeping the lattice parameter constant) would produce the same shifts in the resonance positions as shown in the first row of Table 2. However, if the hole radius is 150 μm, then a 2% change in the hole radius would produce slightly different shifts in the positions of the resonances as shown in the second row of Table 2. Instead of the hole radius, if the lattice parameter is changed by 2%, then the shifts in the resonance positions would again be slightly different (third row of Table 2).

In all cases, a 2% change in either the r/a ratio, the hole radius, or the lattice parameter shifts the positions of the resonances by 2%–3%. In absolute terms, Table 2 suggests that a 5–8 μm change in either the hole radius or the lattice parameter will shift the first three resonances by 10–12 GHz. It will also produce a 4% change in the filling fraction of the holes and change the average refractive index of the slab by <2%. These results indicate the degree of sensitivity of the guided resonances to the crystal parameters.

In Fig. 7(a), all the three resonances have two data points corresponding to $r/a=0.3125$. These data points are obtained from the two crystals that have different individual hole radii and lattice parameters but identical r/a values [Fig. 5 and Fig. 6(b)]. Figure 8 shows a direct comparison between these two spectra. Despite having the same value of r/a and the same slab thickness, the resonances in the transmission spectra of these two crystals do not occur at the same frequencies but show a substantial difference in the spectral positions. Also, the features in the transmission spectra are not identical. We can begin to understand this observation by noting that the t/a ratios are different for the two crystals. Evidently, changes in the value of the slab thickness (normalized with respect to the lattice parameter) can produce changes in the spectral positions of the guided resonances even for crystals with the same r/a values. The r/a ratio still predominantly governs the resonant features since the two crystals display a similar number of resonances within the same bandwidth. It should be noted that the slab thickness of the two samples is identical, and the difference in the t/a value is due to different lattice parameters of the crystals. To study the effect of change in slab thickness on the guided resonances, photonic crystals that differ only in the slab thickness were fabricated.

D. Effect of Change in the Slab Thickness t

Figure 9 shows the transmission spectra of three photonic crystal slabs, each with a different slab thickness t. The hole radius r and the lattice parameter a are identical for all the samples, $r=150$ and $a=400$ μm. The slab thicknesses of the samples are (a) 300, (b) 275, and (c) 250 μm. As the slab thickness decreases, the resonances move to slightly higher frequencies. This is because a decrease in the slab thickness increases the decay length of the

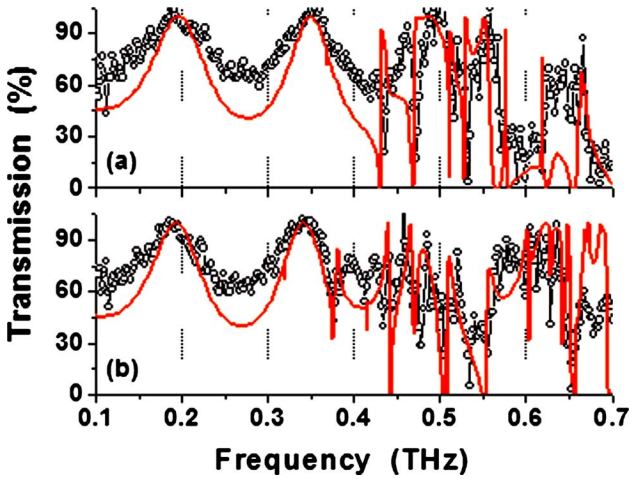

Fig. 8. (Color online) Normal-incidence transmission spectra of photonic crystal slabs with (a) $r=125$, $a=400$ μm and (b) $r=150$, $a=480$ μm. These are the same as Figs. 5(c) and 6(b), respectively. The r/a value and the slab thickness are identical for the two samples, $r/a=0.3125$ and $t=300$ μm. The open circles are experimental results while the solid curves are results of FEM simulations.

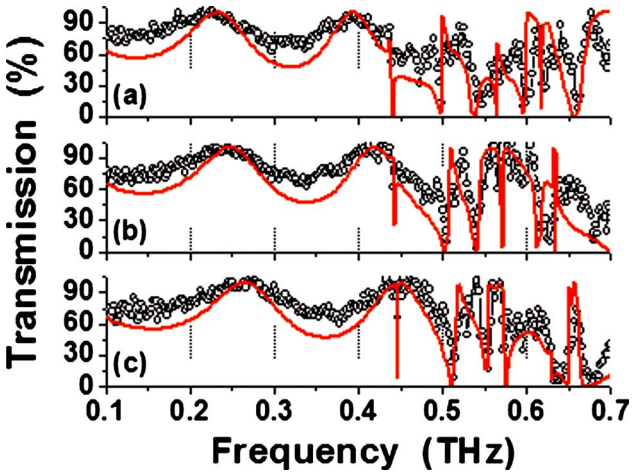

Fig. 9. (Color online) Variation of guided resonances with the slab thickness t. Normal-incidence transmission spectra of photonic crystal slabs with (a) $t=300$, (b) $t=275$, and (c) $t=250\ \mu$m. The hole radius and lattice parameter are identical for all the samples, $r=150$ and $a=400\ \mu$m. The open circles are experimental results while the solid curves are results of FEM simulations.

guided resonance mode, lowering its effective refractive index [44]. As the guided resonance mode leaks out from the center of the slab, it decays exponentially along the direction of the incident radiation. If the slab is thinner, then the decay length in the air region outside the crystal is longer. The effective index experienced by the mode is therefore smaller, causing it to shift toward slightly higher frequencies.

The spectral positions of the resonances can be extracted from Fig. 9. Figure 10 shows the shift in the positions of the first seven resonances as a function of the slab thickness. In general, the resonant frequencies shift toward slightly higher values as the slab thickness is decreased. The observed exceptions are the third and the seventh resonances for the 275 μm thick slab, although these resonances follow the expected trend in the calculated spectra. Such small differences between the experiment and the calculations are not very surprising [27,30,33]. The observed spectral positions of these two resonances deviate from the expected positions by only a very small amount since the rate of shift in the spectral positions of the resonances is very small (on average $\sim$3.6 GHz per 10 μm change in the thickness). Another feature that is evident from Fig. 10 is that the resonant frequencies shift at different rates as the slab thickness is varied. Although the average rate of shift in the resonant frequency is very small, the resonances at higher frequencies tend to shift by larger amounts for similar variations in the slab thickness. Overall, an increase in the slab thickness moves resonances to lower frequencies, causing more resonances to appear within the same bandwidth. Similar theoretical predictions were made in an earlier paper [30].

The coupling strength of a resonance mode can drastically change as the slab thickness is varied. Figure 11 shows the variation in the guided resonances as a function of the slab thickness for samples with $r=150$ and $a=480\ \mu$m. In both the experimental as well as the calculated spectra, the second resonance, clearly evident in the thickest and thinnest slabs just below 0.4 THz, is missing in the 275 μm thick slab. This observation suggests that a change in the slab thickness (to 275 μm) modifies the electric field distribution of the second mode in such a way that it does not couple to the external radiation modes at the frequency, where the resonance should be expected (0.382 THz). The electric field patterns of the modes are known to strongly influence their coupling strengths [30,33,45]. Figure 12 shows the electric field patterns of the second resonance for the three crystals whose transmission spectra are shown in Fig. 11. These two-dimensional plots are obtained from the FEM models. The color indicates the strength of the in-plane electric field, and the arrows denote the local field direction. For slabs with thicknesses of 300 and 250 μm [Figs. 12(a) and 12(c), respectively], this mode has most of the energy concentrated in the air region, facilitating the coupling of the modes to the external radiation field. In contrast, the second mode for the 275 μm thick slab [Fig. 12(b)] has most of its energy concentrated in the dielectric region. This fact evidently inhibits the coupling of this mode to the external field so that it is not observed in the transmission

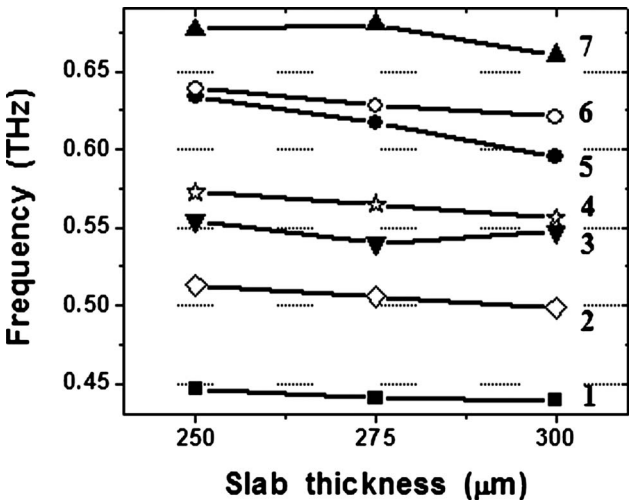

Fig. 10. Shift in the position of the first seven resonances as a function of the slab thickness t (extracted from Fig. 9).

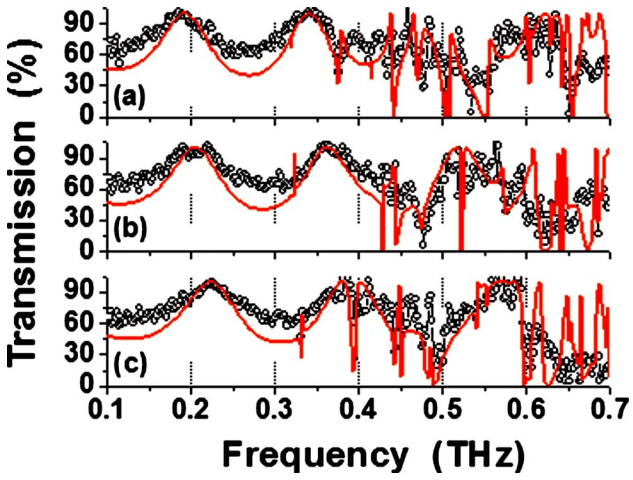

Fig. 11. (Color online) Same as Fig. 9 but for samples with $r=150$ and $a=480\ \mu$m. Slab thicknesses are (a) $t=300$, (b) $t=275$, and (c) $t=250\ \mu$m.

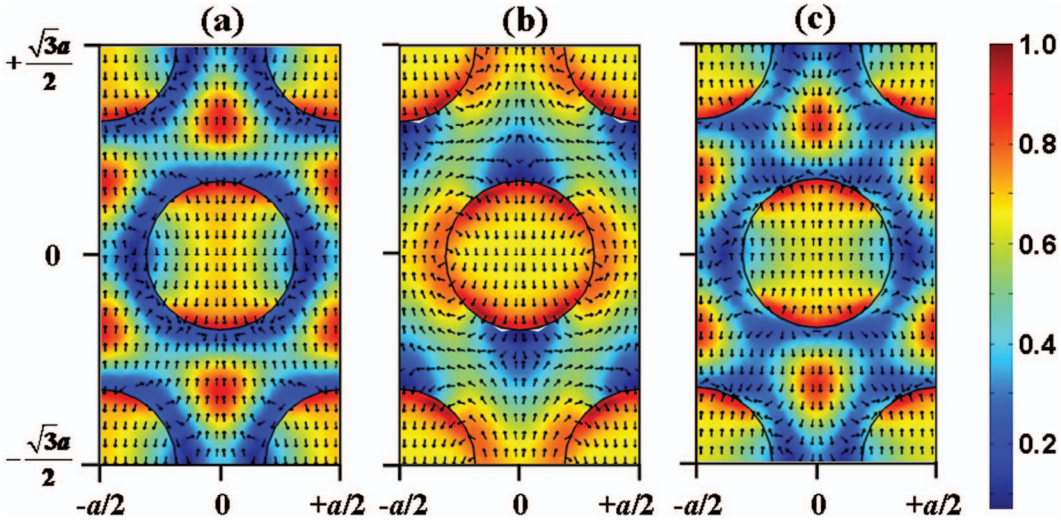

Fig. 12. (Color) Electric field distributions in the planes along half the slab thickness for the three crystals (with $r=150$ and $a=480\ \mu$m) whose transmission spectra are shown in Fig. 11. (a) At 0.375 THz for $t=300\ \mu$m, (b) at 0.382 THz for $t=275\ \mu$m, and (c) at 0.392 THz for $t=250\ \mu$m. The solid black curves depict the hole boundaries, and the arrows denote directions of the in-plane field.

spectrum. It is difficult to make a quantitative statement about the relationship between the degree to which a given mode is excited by an external incident field and the concentration of that mode in the air region, because other considerations (such as the symmetry of the mode) are also relevant. Nevertheless, the trend illustrated in Figs. 11 and 12 is quite general.

Other subtle differences in the spectrum can also appear as the slab thickness is varied. In Fig. 11, the nonuniform shift in the resonant frequencies with respect to the slab thickness is evident from the two resonances between 0.40 and 0.45 THz. While those two resonances can be clearly resolved in the 300 μm thick slab, they almost coalesce into one resonance as the slab thickness is decreased to 250 μm. A variation in the slab thickness also affects the linewidths of the resonances in different ways. As the slab thickness is varied, the linewidth of a particular resonance can either increase or decrease depending on how the electric field symmetry of the mode is modified. For example, the third and fourth resonances (between 0.40 and 0.45 THz) in Fig. 11 become sharper as the slab thickness is decreased. In contrast, the fifth resonance (between 0.45 and 0.50 THz) first becomes broader as the slab thickness is decreased from 300 to 275 μm and then splits into two broader resonances as the slab thickness is further decreased to 250 μm. Figure 13 shows the normal-incidence transmission spectra as a function of the slab thickness for samples with $r=150$ and $a=575\ \mu$m. Again, we observe a resonance (at ~0.3 THz), which clearly becomes broader as the slab thickness is decreased.

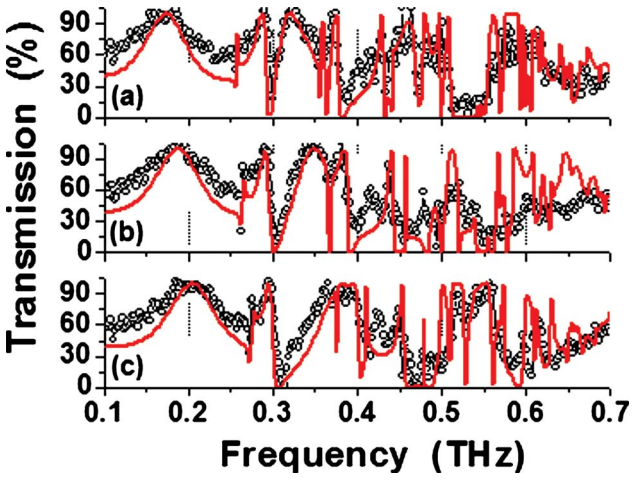

Fig. 13. (Color online) Same as Fig. 9 but for samples with $r=150$ and $a=575\ \mu$m. Slab thicknesses are (a) $t=300$, (b) $t=275$, and (c) $t=250\ \mu$m.

As mentioned in Section 2, terahertz time-domain spectroscopy also provides access to the spectral phase of the transmitted radiation, which can be compared to that of the reference waveform. In the low-frequency range the relative phase increases smoothly, although nonlinearly, with an increase in frequency [46]. At higher frequencies, abrupt jumps corresponding to the guided resonances are observed in the phase spectrum [31]. Figure 14 shows a portion of the phase spectra of the samples whose transmission spectra are shown in Fig. 13, illustrating the abrupt jumps that arise due to the lowest two resonances. The positions of the sudden jumps correspond to the positions of the guided resonances. Their shift to slightly higher frequencies with the decrease in slab thickness is consistent with the earlier observed trend.

From the various transmission spectra, we see that the asymmetrical transmission line shapes of the guided resonances manifest themselves in very distinct ways. For example, in the lowest resonances shown in Fig. 13 (just above 0.25 THz), the transmission first drops to lower values and then jumps to higher values as the frequency increases across the resonance. In contrast, for the lowest resonances shown in Fig. 9 (just below 0.45 THz), the transmission first becomes higher and then drops to a smaller value as the frequency increases across the resonance. These two different variations in the transmission line shapes of guided resonances have been proposed for a bistable optical transfer [47] and require resonances with very narrow linewidths.

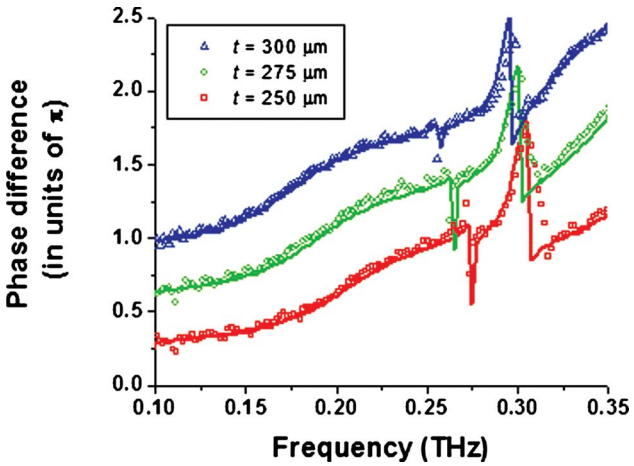

Fig. 14. (Color online) Portion of the relative phase spectrum for the three crystals (with $r=150$ and $a=575$ μm) whose transmission spectra are shown in Fig. 14. The symbols are experimental results, while the solid curves are the corresponding FEM simulations. The results for $t=300$ and $t=275$ μm are vertically offset for clarity.

For an accurate estimate of the linewidth with very sharp resonances, we analyze the transmission line shapes of the lowest resonances shown in Fig. 9 (just below 0.45 THz) using our FEM simulation with a higher frequency resolution of 0.1 GHz. The result is shown in Fig. 15(a). These simulations reveal that the line shapes can change dramatically as the slab thickness changes. For the 250 μm slab, we predict a symmetrical line with a width of ~380 MHz, corresponding to a Q factor of more than 1100. For the thicker slabs, we observe that the line shapes become increasingly asymmetric. This is a manifestation of the fact that the line shapes become symmetrical and the structure behaves as a narrowband reflector if the corresponding direct pathway transmission (Fabry–Perot response) is 100% as described by Fan and Joannopoulos [14].

We were not able to spectrally resolve these narrow spectral features with our time-domain spectroscopic technique, so instead we relied on a different spectrometer to characterize these specific features. We used a transmission spectrometer based on a BWO operating in the 100–180 GHz range [48,49]. A frequency tripler based on a planar GaAs Schottky diode is used to shift the BWO output to the higher frequency range required for these measurements [50]. The radiation transmitted through the sample is detected using a Golay cell. The results for two photonic crystal samples are shown in Fig. 15(b). To avoid standing-wave effects, the sample was tilted at a small angle relative to the axis of the terahertz beam. This may explain the small frequency shift of the measurements relative to the simulations as well as the slight broadening of the resonances. Nevertheless, the measurements closely resemble the corresponding simulations in Fig. 15(a), in particular the ~6 GHz shift to a lower frequency for the thicker slab as well as the change from a nearly symmetrical to a strongly asymmetrical line shape.

6. TRANSMISSION SPECTRA OF CRYSTALS WITH SQUARE LATTICES

The results presented in Sections 2–5 are for photonic crystal slabs with a hexagonal lattice of air holes. A photonic crystal slab with a square lattice of holes was also fabricated to study the effect of a lattice structure on the guided resonances. The crystal parameters of this sample are $r=180$, $a=400$, and $t=300$ μm. Figure 16 shows the FEM model used to calculate the normal-incidence trans-

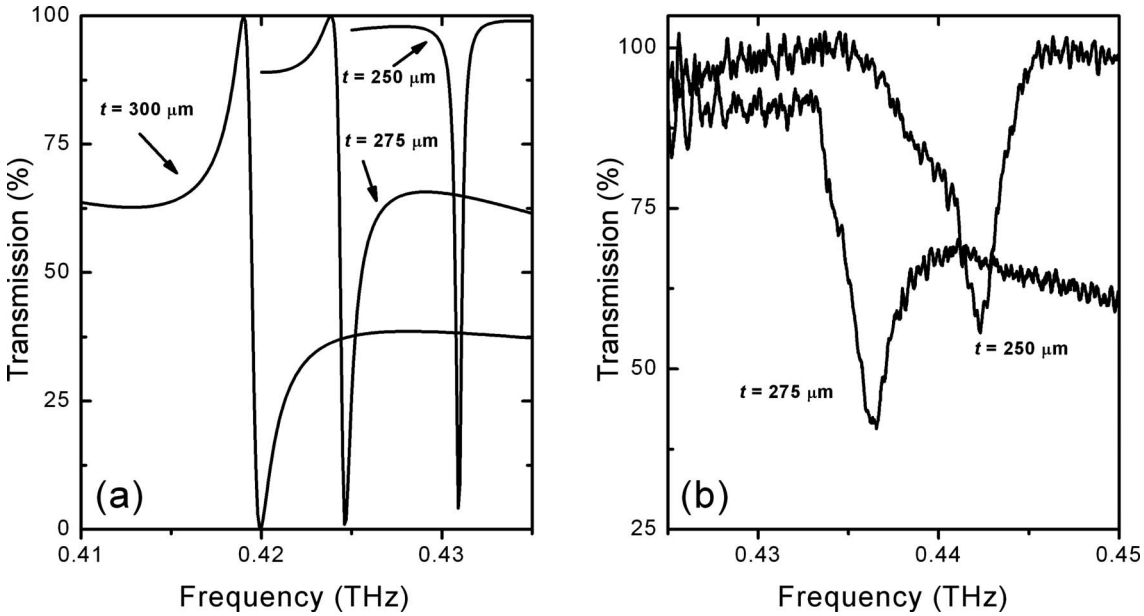

Fig. 15. (a) High-resolution calculation of the line shape of the lowest-frequency resonance for three different values of the slab thickness for a photonic crystal slab with $r=150$ and $a=400$ μm (as in Fig. 10). A frequency resolution of 0.1 GHz is used in the FEM simulations. For the 250 μm thick slab, the resonance is quite narrow (~380 MHz) with a Q-factor in excess of 1100. (b) Measured transmission spectra for two samples corresponding to two of the curves in (a). These measurements were performed using a BWO source with a spectral resolution below 1 GHz.

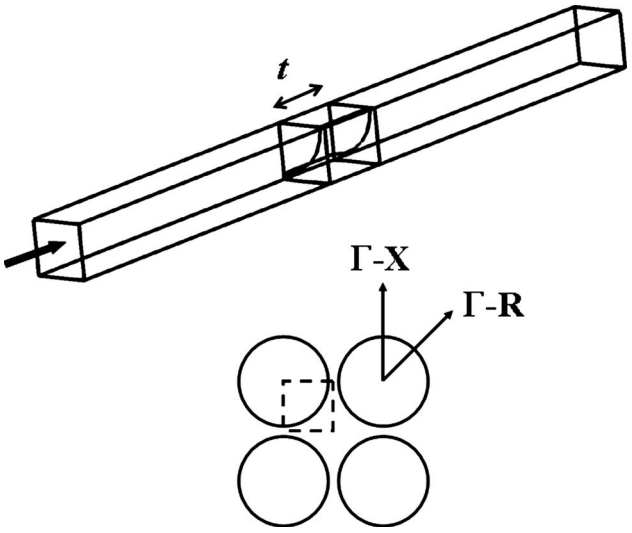

Fig. 16. Same as Fig. 3 but for a square lattice.

mission spectrum of the square lattice photonic crystal slab. It is similar to the computational domain of the hexagonal lattice crystal (Fig. 3) except for the unit cell geometry. As the unit cell of the square lattice crystal is smaller in size in comparison to the hexagonal lattice crystal, discretization of the computational domain with a 20 μm mesh size results in a model with fewer mesh elements (~400,000). The electric field is polarized along the Γ-X direction of the lattice, and the normal-incidence transmission coefficient is obtained by taking the ratio of the integrated power at the output plane to that at the input plane.

Figure 17 shows the transmission spectra of photonic crystal slabs with hexagonal and square lattices. Both samples have identical crystal parameters, $r=180$, $a=400$, and $t=300$ μm. However, as the lattice structures are different, the filling fraction of holes is much lower in the square lattice (63.6%) in comparison to the hexagonal lattice (73.5%). Consequently, the average refractive index of the square lattice photonic crystal slab is higher, causing the resonances to appear at lower frequencies.

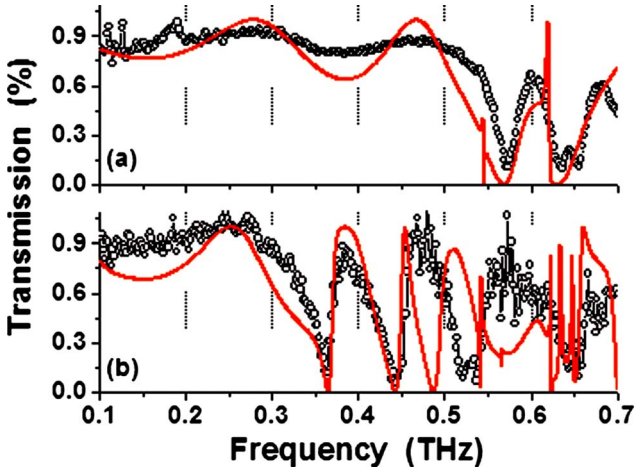

Fig. 17. (Color online) Normal-incidence transmission spectra of photonic crystal slabs with (a) hexagonal and (b) square lattices. The crystal parameters are identical for the two samples, $r=180$, $a=400$, and $t=300$ μm. The open circles are experimental results while the solid curves are results of FEM simulations.

7. CONCLUSIONS

In summary, the normal-incidence transmission spectra of photonic crystal slabs with air holes in silicon have been measured using terahertz time-domain spectroscopy and calculated using finite element simulations. The Fano line shapes of the resonant features in the transmission spectrum can be described by a simple analytical model that considers coupling of discrete and continuum modes of the photonic crystal slab. The variations in the spectral positions of these resonant features were studied as a function of crystal parameters such as the hole radius, lattice parameter, and slab thickness. The transmission spectrum of a photonic crystal slab with a hexagonal lattice of holes was also compared to that of a photonic crystal slab with a square lattice of holes.

The spectral positions of the resonances are most sensitive to changes in the r/a ratio, which changes the average refractive index of the slab. Observations show that the resonances are quite sensitive to the hole radius and the lattice parameter, and even a small 2% change in either of the parameters can shift the spectral position of the resonances slightly and change the line shape. In contrast, the shifts in the positions and line shapes of the resonances are relatively smaller, although still not negligible, for variations in the slab thickness. In general, increasing the slab thickness moves the resonances to slightly lower frequencies, causing more resonances to appear within the same bandwidth. A change in the slab thickness can also increase or decrease the lifetimes of the modes. A comparison of the transmission spectra of slabs with identical structural parameters but different lattice structures (square and hexagonal) shows that the occurrence of resonant features at relatively lower frequencies in the square lattice can be understood by considering the effects of the average refractive index. These results should inspire further interest in the development of photonic devices based on guided resonances.

ACKNOWLEDGMENTS

This work has been supported in part by the National Science Foundation and the Robert A. Welch Foundation. The authors thank Jonathan Laib and Hui Zhan for assistance with the terahertz spectrometer. We also thank Vladimir Koslov and Walter Hurlbut from Microtech Instruments, Inc., for assistance in obtaining the high-resolution data shown in Fig. 15(b).

REFERENCES

1. J. D. Joannopoulos, R. D. Meade, and J. N. Winn, *Photonic Crystals: Molding the Flow of Light* (Princeton U. Press, 1995).
2. K. Sakoda, *Optical Properties of Photonic Crystals* (Springer, 2001).
3. S. G. Johnson and J. D. Joannopoulos, *Photonic Crystals: The Road from Theory to Practice* (Springer, 2002).
4. E. Chow, S. Y. Lin, S. G. Johnson, P. R. Villeneuve, J. D. Joannopoulos, J. R. Wendt, G. A. Vawter, W. Zubrzycki, H.

Hou, and A. Alleman, "Three-dimensional control of light in a two-dimensional photonic crystal slab," Nature **407**, 983–986 (2000).
5. A. Mekis, J. C. Chen, I. Kurland, S. H. Fan, P. R. Villeneuve, and J. D. Joannopoulos, "High transmission through sharp bends in photonic crystal waveguides," Phys. Rev. Lett. **77**, 3787–3790 (1996).
6. S. G. Johnson, S. H. Fan, P. R. Villeneuve, J. D. Joannopoulos, and L. A. Kolodziejski, "Guided modes in photonic crystal slabs," Phys. Rev. B **60**, 5751–5758 (1999).
7. S. G. Johnson, P. R. Villeneuve, S. H. Fan, and J. D. Joannopoulos, "Linear waveguides in photonic-crystal slabs," Phys. Rev. B **62**, 8212–8222 (2000).
8. R. Moussa, S. Foteinopoulou, L. Zhang, G. Tuttle, G. T. K. Guven, E. Ozbay, and C. M. Soukoulis, "Negative refraction and superlens behavior in a two-dimensional photonic crystal," Phys. Rev. B **71**, 085106 (2005).
9. S. N. Tandon, M. Soljačić, G. S. Petrich, J. D. Joannopoulos, and L. A. Kolodziejski, "The superprism effect using large area 2D-periodic photonic crystal slabs," Photon. Nanostruct. Fundam. Appl. **3**, 10–18 (2005).
10. P. T. Rakich, M. S. Dahlem, S. Tandon, M. Ibanescu, M. Soljacic, G. S. Petrich, J. D. Joannopoulos, L. A. Kolodziejski, and E. P. Ippen, "Achieving centimetre-scale supercollimation in a large-area two-dimensional photonic crystal," Nat. Mater. **5**, 93–96 (2006).
11. T. Matsumoto, T. Asatsuma, and T. Baba, "Experimental demonstration of a wavelength demultiplexer based on negative-refractive photonic-crystal components," Appl. Phys. Lett. **91**, 091117 (2007).
12. M. Kanskar, P. Paddon, V. Pacradouni, R. Morin, A. Busch, J. F. Young, S. R. Johnson, J. MacKenzie, and T. Tiedje, "Observation of leaky slab modes in an air-bridged semiconductor waveguide with a two-dimensional photonic lattice," Appl. Phys. Lett. **70**, 1438–1440 (1997).
13. V. N. Astratov, I. S. Culshaw, R. M. Stevenson, D. M. Whittaker, M. S. Skolnick, T. F. Krauss, and R. M. De la Rue, "Resonant coupling of near-infrared radiation to photonic band structure waveguides," J. Lightwave Technol. **17**, 2050–2057 (1999).
14. S. H. Fan and J. D. Joannopoulos, "Analysis of guided resonances in photonic crystal slabs," Phys. Rev. B **65**, 235112 (2002).
15. S. H. Fan, W. Suh, and J. D. Joannopoulos, "Temporal coupled-mode theory for the Fano resonance in optical resonators," J. Opt. Soc. Am. A **20**, 569–572 (2003).
16. U. Fano, "Effects of configuration interaction on intensities and phase shifts," Phys. Rev. **124**, 1866–1878 (1961).
17. A. R. P. Rau, "Perspectives on the Fano resonance formula," Phys. Scr. **69**, C10–C13 (2004).
18. A. A. Erchak, D. J. Ripin, S. Fan, P. Rakich, J. D. Joannopoulos, E. P. Ippen, G. S. Petrich, and L. A. Kolodziejski, "Enhanced coupling to vertical radiation using a two-dimensional photonic crystal in a semiconductor light-emitting diode," Appl. Phys. Lett. **78**, 563–565 (2001).
19. H. Y. Ryu, Y. H. Lee, R. L. Sellin, and D. Bimberg, "Over 30-fold enhancement of light extraction from free-standing photonic crystal slabs with InGaAs quantum dots at low temperature," Appl. Phys. Lett. **79**, 3573–3575 (2001).
20. M. Fujita, S. Takahashi, Y. Tanaka, T. Asano, and S. Noda, "Simultaneous inhibition and redistribution of spontaneous light emission in photonic crystals," Science **308**, 1296–1298 (2005).
21. V. Lousse, W. Suh, O. Kilic, S. Kim, O. Solgaard, and S. H. Fan, "Angular and polarization properties of a photonic crystal slab mirror," Opt. Express **12**, 1575–1582 (2004).
22. A. E. Miroshnichenko and Y. S. Kivshar, "Sharp bends in photonic crystal waveguides as nonlinear Fano resonators," Opt. Express **13**, 3969–3976 (2005).
23. W. Suh, M. F. Yanik, O. Solgaard, and S. H. Fan, "Displacement-sensitive photonic crystal structures based on guided resonance in photonic crystal slabs," Appl. Phys. Lett. **82**, 1999–2001 (2003).
24. W. Suh and S. H. Fan, "Mechanically switchable photonic crystal filter with either all-pass transmission or flat-top reflection characteristics," Opt. Lett. **28**, 1763–1765 (2003).
25. Y. Kanamori, T. Kitani, and K. Hane, "Control of guided resonance in a photonic crystal slab using microelectromechanical actuators," Appl. Phys. Lett. **90**, 031911 (2007).
26. A. Rosenberg, M. W. Carter, J. A. Casey, M. Kim, R. T. Holm, R. L. Henry, C. R. Eddy, V. A. Shamamian, K. Bussmann, S. Shi, and D. W. Prather, "Guided resonances in asymmetrical GaN photonic crystal slabs observed in the visible spectrum," Opt. Express **13**, 6564–6571 (2005).
27. O. Kilic, S. Kim, W. Suh, Y. A. Peter, A. S. Sudbo, M. F. Yanik, S. H. Fan, and O. Solgaard, "Photonic crystal slabs demonstrating strong broadband suppression of transmission in the presence of disorders," Opt. Lett. **29**, 2782–2784 (2004).
28. T. Prasad, V. L. Colvin, and D. M. Mittleman, "The effect of structural disorder on guided resonances in photonic crystal slabs studied with terahertz time-domain spectroscopy, Opt. Express **15**, 16954–16965 (2007).
29. V. Pacradouni, W. J. Mandeville, A. R. Cowan, P. Paddon, J. F. Young, and S. R. Johnson, "Photonic band structure of dielectric membranes periodically textured in two dimensions," Phys. Rev. B **62**, 4204–4207 (2000).
30. K. B. Crozier, V. Lousse, O. Kilic, S. Kim, S. H. Fan, and O. Solgaard, "Air-bridged photonic crystal slabs at visible and near-infrared wavelengths," Phys. Rev. B **73**, 115126 (2006).
31. Z. P. Jian and D. M. Mittleman, "Characterization of guided resonances in photonic crystal slabs using terahertz time-domain spectroscopy," J. Appl. Phys. **100**, 123113 (2006).
32. J. F. Song, R. P. Zaccaria, M. B. Yu, and X. W. Sun, "Tunable Fano resonance in photonic crystal slabs," Opt. Express **14**, 8812–8826 (2006).
33. C. Grillet, D. Freeman, B. Luther-Davies, S. Madden, R. McPhedran, D. J. Moss, M. J. Steel, and B. J. Eggleton, "Characterization and modeling of Fano resonances in chalcogenide photonic crystal membranes," Opt. Express **14**, 369–376 (2006).
34. M. van Exter and D. R. Grischkowsky, "Characterization of an optoelectronic terahertz beam system," IEEE Trans. Microwave Theory Tech. **38**, 1684–1691 (1990).
35. Z. P. Jian, J. Pearce, and D. M. Mittleman, "Two-dimensional photonic crystal slabs in parallel-plate metal waveguides studied with terahertz time-domain spectroscopy," Semicond. Sci. Technol. **20**, S300–S306 (2005).
36. T. Prasad, V. L. Colvin, Z. Jian, and D. M. Mittleman, "Superprism effect in a metal-clad terahertz photonic crystal slab," Opt. Lett. **32**, 683–685 (2007).
37. N. Jukam and M. S. Sherwin, "Two-dimensional terahertz photonic crystals fabricated by deep reactive ion etching in Si," Appl. Phys. Lett. **83**, 21–23 (2003).
38. C. Yee, N. Jukam, and M. Sherwin, "Transmission of single mode ultrathin terahertz photonic crystal slabs," Appl. Phys. Lett. **91**, 194104 (2007).
39. D. Grischkowsky, S. Keiding, M. Vanexter, and C. Fattinger, "Far-infrared time-domain spectroscopy with terahertz beams of dielectrics and semiconductors," J. Opt. Soc. Am. B **7**, 2006–2015 (1990).
40. W. Axmann and P. Kuchment, "An efficient finite element method for computing spectra of photonic and acoustic band-gap materials: I. Scalar case," J. Comp. Physiol. **150**, 468–481 (1999).
41. W. R. Frei and H. T. Johnson, "Finite-element analysis of disorder effects in photonic crystals," Phys. Rev. B **70**, 165116 (2004).
42. J. A. Deibel, N. Berndsen, K. Wang, and D. M. Mittleman, "Frequency-dependent radiation patterns emitted by THz plasmons on finite length cylindrical metal wires," Opt. Express **14**, 8772–8778 (2006).
43. J. Deibel, M. Escarra, N. Berndsen, K. Wang, and D. M. Mittleman, "Finite element method simulations of guided wave phenomena at terahertz frequencies," Proc. IEEE **95**, 1624–1640 (2007).

44. W. Suh, O. Solgaard, and S. Fan, "Displacement sensing using evanescent tunneling between guided resonances in photonic crystal slabs," J. Appl. Phys. **98**, 033102 (2005).
45. T. Ochiai and K. Sakoda, "Dispersion relation and optical transmittance of a hexagonal photonic crystal slab," Phys. Rev. B **63**, 125107 (2001).
46. Z. Jian and D. M. Mittleman, "Out-of-plane dispersion and homogenization in photonic crystal slabs," Appl. Phys. Lett. **87**, 191113 (2005).
47. V. Lousse and J. P. Vigneron, "Use of Fano resonances for bistable optical transfer through photonic crystal films," Phys. Rev. B **69**, 155106 (2004).
48. G. Kozlov and A. Volkov, "Coherent source submillimeter wave spectroscopy," in *Millimeter and Submillimeter Wave Spectroscopy of Solids*, G. Grüner, ed. (Springer-Verlag, 1998).
49. B. Gorshunov, A. Volkov, I. Spektor, A. Prokhorov, A. Mukhin, M. Dressel, S. Uchida, and A. Loidl, "Terahertz BWO spectroscopy," Int. J. Infrared Millim. Waves **26**, 1217–1240 (2005).
50. T. W. Crowe, D. W. Porterfield, J. L. Hesler, W. L. Bishop, D. S. Kurtz, and K. Hui, "Terahertz technology for imaging and spectroscopy," Proc. SPIE **6212**, 62120V (2006).